Performance enhancement of Wells turbine: Combined radiused edge blade tip, static extended trailing edge, and variable thickness modifications

P. Madhan Kumar [a], Paresh Halder [a, b], Afzal Husain [c], Abdus Samad [a, *]

[a] *Wave Energy and Fluids Engineering Lab, Ocean Engineering Department, IIT Madras, Chennai, 600036, India*
[b] *Quantum Wave Microscopy Unit, Okinawa Institute of Science and Technology Graduate University, 1919-1 Tancha, Onna-son, Okinawa, 904-0495, Japan*
[c] *Department of Mechanical and Industrial Engineering, Sultan Qaboos University, PO Box 33, Al-Khoudh, PC-123, Muscat, Sultanate of Oman*

ARTICLE INFO

ABSTRACT

The Wells turbine is used in conjunction with an oscillating water column to harvest wave energy. It is a self-rectifying axial flow reaction turbine which consists of symmetrical blades aligned normal to the incoming flow. A narrow operating range due to flow separation restricts the power extracting capability of the turbine at a higher flow rate. To improve its performance, a turbine blade with combined design modifications such as radiused edge blade (REB) tip, static extended trailing edge (SETE) and variable thickness blade (VTB) was investigated through CFD analysis. Three-dimensional time independent Reynolds-averaged Navier-Stokes equations were solved in a commercial solver to obtain the turbine performance, which was given by non-dimensional torque, pressure drop and efficiency. The combined REB tip, SETE and VTB modifications enhanced relative average turbine power output by 97% and the relative operating range by 22%. However, the average efficiency is decreased by 7.7%, because of the increased pressure drop.

Nomenclature

Abbreviations

AR	Aspect ratio
LE	Leading edge
OWC	Oscillating water column
PS	Pressure side
PTO	Power take-off
RANS	Reynolds-averaged Navier-Stokes
RET	Radiused edge tip
SETE	Static extended trailing edge
SS	Suction side
SST	Shear stress transport
TE	Trailing edge
TLF	Tip leakage flow
TLV	Tip leakage vortex
VTB	Variable thickness blade
WEC	Wave energy converter

Symbols

C Cp	Chord length [mm] Pressure coefficient [-]
Cp_{tot}	Total pressure coefficient [-]

h	Average cell size [m^3]
$H = \frac{R_{hub}}{R_{tip}}$	Hub to tip ratio [-]
k	Turbulence kinetic energy [m^2/s^2]
p	Pressure [Pa]
$\Delta p = p_i - p_e$	Pressure drop [Pa]
$\Delta p^* = \frac{\Delta p}{\rho \omega^2 R_{tip}^2}$	Pressure drop coefficient [-]
Q	Volume flow rate [m^3/s]
R_{hub}	Blade hub radius [mm]
$R_{mid} = \frac{(R_{tip}+R_{hub})}{2}$	Radius of blade midspan [mm]
R_{tip}	Blade tip radius [mm]
T	Torque [$N·m$]
$T^* = \frac{T}{\rho \omega^2 R_{tip}^5}$	Torque coefficient [-]
U_A	Inlet axial velocity [m/s]
U_{tip}	Blade tip velocity [m/s]
$U^* = \frac{U_A}{U_{tip}}$	Flow coefficient [-]
V	Absolute velocity [m/s]
W	Relative velocity [m/s]
y^+	Non-dimensional wall distance [-]

* Corresponding author.
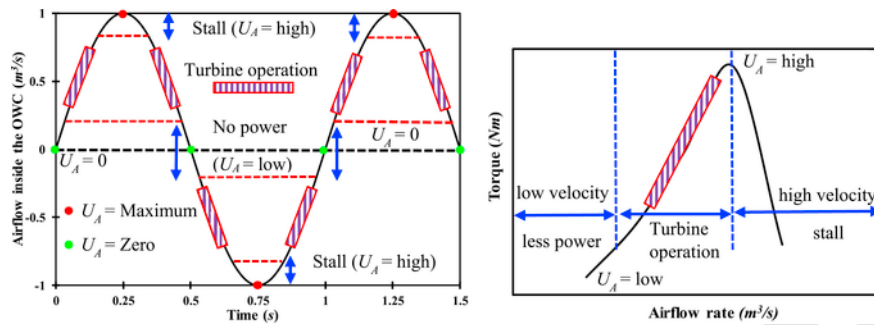   *Email address:* samad@iitm.ac.in (A. Samad).

Fig. 1. Airflow inside the OWC (left) and torque characteristic of Wells turbine (right).
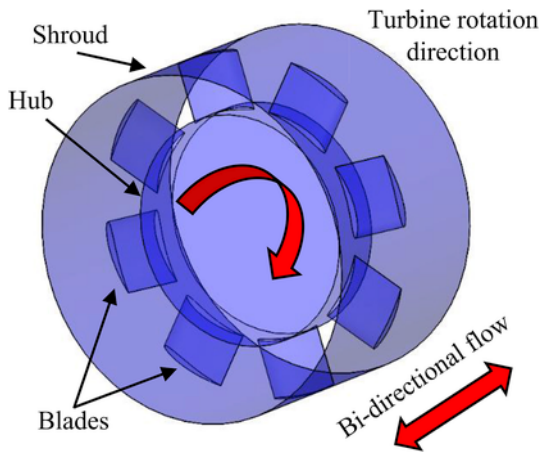

Fig. 2. Schematic of Wells turbine.

Table 1
Turbine specification (Torresi et al., 2008).

Blade airfoil profile	NACA 0015
No of blades	8
Chord length (C)	125 mm
Hub radius	200 mm
Tip radius	300 mm
Mean radius	250 mm
Hub to tip ratio	0.6667
Solidity at mean radius	0.64
Tip clearance	1.25 mm
Rotational speed	2000 rpm

Z	Number of blades [-]
α	Angle of attack [°]
ρ	Density [kg/m^3]
Ω	Angular velocity [rad/s]
$\eta = \dfrac{T\omega}{Q\Delta p_o}$	Efficiency [-]

Subscripts

1, i	Inlet
2, e	Outlet
o	Stagnation
t	Tangential

1. Introduction

The ocean wave energy has a huge potential to meet our ever-growing energy demands and to reduce dependency on fossil fuels. The energy is available throughout the year and easily predictable. However, its commercial extraction has many hindrances such as harsh environment, high cost and low performance, etc. Increasing the performance of wave energy converter (WECs) is inevitable for economically viable power extraction (Astariz and Iglesias., 2015). The oscillation water column (OWC) device is the most commonly used WEC (Mustapa et al., 2017). It consists of a partially submerged concrete structure with an opening below the water surface, which creates an air chamber. The incoming wave compresses and decompresses the entrapped air by oscillating motion and the air turbine inside the OWC extracts energy from the airflow. Wells turbine is one of the most commonly used air turbines in an OWC device (Falcão, 2010). It is a self-rectifying axial reaction turbine and consists of symmetrical airfoil blades. The merits of Wells turbine include low cost, high blade velocity for relatively low airflow velocity and simple to construct; whereas its demerits are noisy operation, reduced torque at small flow rates and a narrow operating range (Falcão., 2010).

To understand the Wells turbine operation, airflow inside the OWC and the turbine torque characteristic are illustrated in Fig. 1. The airflow inside the OWC is cyclic in nature and varies from a maximum to a minimum value, and vice versa. At low air flowrate, there is no power generation due to low air velocity; whereas at high flowrate, stall occurs due to high air velocity. Despite the availability of high power at higher flowrate, the stall phenomenon restricts the ability of turbine to extract energy. Hence, the power extracted by the Wells turbine is intermittent in nature and to improve its performance, the power extracting capability of turbine at low velocity and the operating range should be improved. An exhaustive study on the various design parameters affecting the performance of Wells turbine can be found in the works of Raghunathan (1995) and Shehata et al. (2017). The Wells turbine performance is very sensitive to tip clearance (Raghunathan, 1995) and tip leakage flow (TLF) (Taha et al., 2011). A higher value of tip clearance delays stall with reduced efficiency; in contrast, small tip clearance improves efficiency and advances the stall (Raghunathan, 1995).

Researchers investigated various configuration such as bi-plane (Raghunathan and Tan, 1983), guide vanes (Gato, 1990), contra-rotating (Raghunathan and Beattie, 1996), blade sweep (Gato and Webster, 2001), variable chord (Govardhan and Dhanasekaran, 2002) and optimized airfoil profiles (Mohamed et al., 2011; Shaaban, 2017) to improve the Wells turbine performance. As discussed earlier, the TLF affects the performance of Wells turbine significantly. Takao et al. (2007) implemented end plates to suppress the TLF, whereas Taha et al. (2011) proposed a non-uniform tip clearance to enhance the performance. Shaaban and Hafiz (2012) optimized the duct geometry to improve the turbine power and efficiency. The optimized design weakened the mixing between TLF and blade suction side (SS) flow and improved the performance. Halder et al. (2015) adopted a casing groove to delay the stall phenomenon by altering the TLF behavior. Cui et al. (2016) studied various blade tip configurations to improve performance and found that the ring type blade performed relatively better. Halder et al. (2017) and Halder et al. (2018) optimized the blade sweep angle with thickness and casing groove to augment the turbine power and to delay stall. Nazeryan and Lakzian (2018) studied variable

Table 2
Reference blade and variants of blade modifications.

Design	Blade geometry		
	Front view	Top view	Side view
Reference blade		Sharp edge tip	Constant thickness
VTB			Variable thickness
RETB	Radiused edge tip	Radiused edge tip	
SETE		SETE	
VTB + RETB	Radiused edge tip SETE	Radiused edge tip	Variable thickness
VTB + SETE		SETE	Variable thickness
RETB + SETE	Radiused edge tip SETE SETE	Radiused edge tip SETE	
VTB + RETB + SETE	Radiused edge tip SETE	Radiused edge tip SETE	Variable thickness
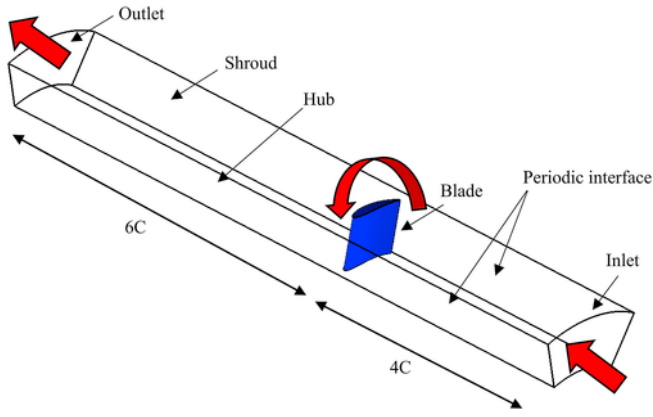
Fig. 3. Flow domain with single blade and periodic interfaces.

thickness distribution from hub to tip and reported that the variable thickness blade (VTB) diminished the mixing between the TLF and blade SS flow. The VTB reduced the entropy generation and improved stall characteristics. A similar phenomenon of the TLF modification is presented in the study of Kumar et al. (2018). They introduced a radiused edge tip (RET) blade to alter the TLF pattern that improved the relative peak turbine power and operating range by 37% and 25%, respectively.

From the above discussion, it can be concluded that the nature of interaction between the TLF and the primary flow on the blade SS dictates the aerodynamic performance of Wells turbine. Various authors used different design modifications to weaken the above-said interactions; however, the combined effects of these proven design modifications were not investigated. Moreover, Liu et al. (2007) observed that the airfoil with static extended trailing edge (SETE) enhances the lift coefficient. The idea of SETE was inspired from the thin extended trailing edge found in the birds such as owl and merganser (Liu et al., 2006). In a quest to enhance the Wells turbine performance by increasing the operating range and turbine power, the combined effects of blade modifications such as VTB, RETB, and SETE are investigated in this study. It is evident from the literature that both VTB and RETB has increased the operating range, whereas SETE is anticipated to improve the turbine power. The aerodynamic performance of the modified blades is obtained by solving the three-dimensional steady Reynolds-averaged Navier-Stokes (RANS) equation and compared with the reference blade. An extensive parametric analysis and discussion are provided by analysing the flow behavior to unveil the aerodynamic effects of the modified blades.

1.1. Description of reference and modified blades

The reference Wells turbine geometry is presented in Fig. 2, and the specifications are given in Table 1 (Torresi et al., 2008). A combination of VTB, RETB and SETE are modified to generate seven different blades (Table 2). The blade tip, trailing edge (TE) and thickness distributions are altered and new designs are produced. In case of VTB, NACA 0010, NACA 0015 and NACA 0020 profiles are implemented at the hub, midspan and tip, respectively (Nazeryan and Lakzian, 2018). The RETB is created using the fillet option in SolidWorks (Dassault Systems, Waltham, MA), with a radius of 1%C as reported in the study of Kumar et al. (2018). The SETE is implemented by fixing the leading edge (LE) and extending TE without altering the original features of the airfoil. The length (l), thickness (t) and deflection are fixed as 5%C, 0.25 mm and 0°, respectively (Liu et al., 2007).

2. Performance parameters

The turbine performance can be expressed as:
Torque coefficient (T^*)

$$T^* = \frac{T}{\rho \omega^2 R_{tip}^5} \tag{1}$$

Static pressure drop coefficient (Δp^*)

$$\Delta p^* = \frac{\Delta p}{\rho \omega^2 R_{tip}^2} \tag{2}$$

Efficiency (η)

$$\eta = \frac{T\omega}{Q\Delta p} \tag{3}$$

Flow coefficient (U^*)

$$U^* = \frac{U_A}{U_{tip}} \tag{4}$$

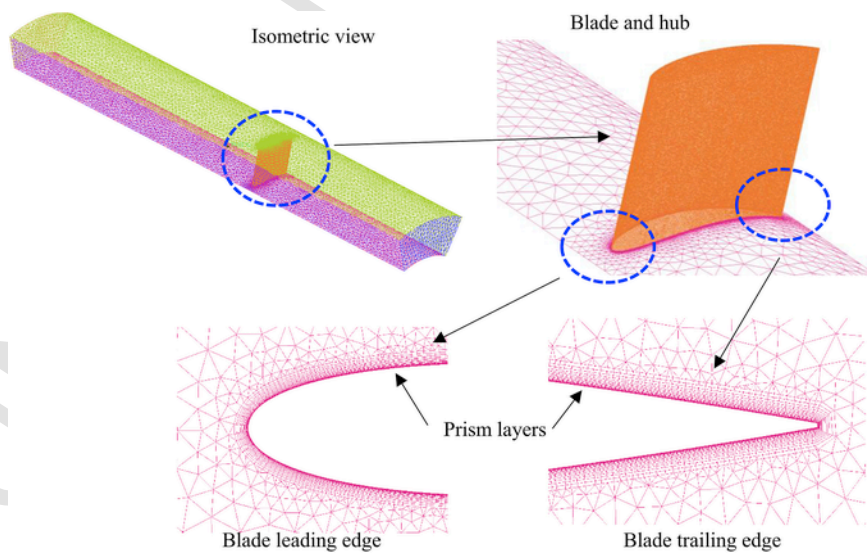**Fig. 4.** Discretized computational domain.

Table 3
Numerical model and applied conditions.

Working fluid	Air
Type of analysis	Steady
Nature of flow	Incompressible
Computational domain	Single blade with periodic interface
Rotation speed	2000 rpm
Inlet	Axial velocity (4–18 m/s)
Outlet	Zero relative pressure
Blade and hub	No-slip wall
Shroud	No-slip counter rotating wall
Lateral sides	Periodic boundary
Reference pressure	1 atm
Turbulence intensity	5%
Advection scheme	High-resolution

Table 4
Grid parameters and Grid Convergence Index (GCI) analysis.

Number of elements (10^6)	N_1, N_2, N_3	6.80, 3.07, 1.39
Average grid size (h)	h_1, h_2, h_3	0.0052, 0.0068, 0.0089
Grid refinement factor (r)	r_{21}, r_{32}	1.3, 1.3
Performance parameter (φ)	φ_1, φ_2, φ_3	0.0427, 0.0422, 0.0402
Apparent order	P	5.47
Extrapolated values	φ_{ext}^{12}, φ_{ext}^{32}	0.04294, 0.04295
Approximate relative error	e_a^{21}, e_a^{32}	1.14%, 4.95%
Extrapolated relative error	e_{ext}^{21}, e_{ext}^{32}	0.35%, 1.52%
GCI	GCI_{fine}^{21}, GCI_{medium}^{32}	0.43%, 1.92%

Table 5
Flow coefficient and inlet axial velocity flow ranges.

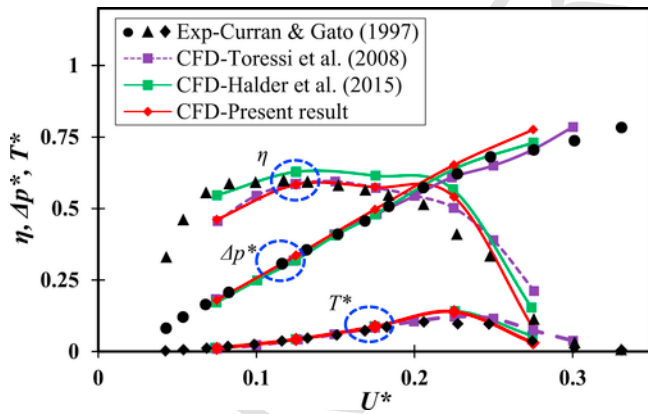| Flow coefficient (U^*) [-]	Inlet axial velocity (U_A) [m/s]
0.075	4.712
0.125	7.854
0.175	10.996
0.225	14.137
0.275	17.279

Fig. 5. Validation of present numerical model with published data for η, Δp^*, and T^*.

3. Numerical methodology

The numerical analyses were performed by solving steady incompressible RANS equation. The two-equation eddy viscosity-based, k-ω shear stress transport (SST) was chosen as the turbulence closure model; since it is favourable for flows with adverse pressure gradient and separation. It is a blend of k-ε and k-ω model, which compensates the limitation of both models by applying k-ω model in the near wall region and k-ε in region away from the wall (Menter, 1994). The k-ω SST turbulence model is mesh sensitive and requires a fine mesh with y^+ value less than one to resolve the viscous sublayer region near the wall (Ansys CFX, 2011).

Fig. 3 displays the flow domain used for the numerical study. The upstream and downstream lengths of the flow domain were fixed as 4 and 6 times of chord length, respectively (Torresi et al., 2009; Halder et al., 2015; Hu and Li, 2018). A Cartesian coordinate system was adopted such that the x, y, and z-axes represent chordwise, streamwise and spanwise directions, respectively. A rotating frame of reference was used to realize the rotational effects of turbine without physically rotating it. Additional momentum sources are added to governing equations to account for the Coriolis and the centrifugal force components (Ansys CFX, 2011). The flow domain was meshed with unstructured tetrahedral elements in ICEM CFD 15.0 (Fig. 4) (Ansys ICEM CFD, 2012). Additionally, prism elements with an initial height of 0.011 mm and a height ratio of 1.2, were created around the blade to resolve the boundary layer. The details of boundary conditions are provided in Table 3. The numerical simulations were carried out using Ansys CFX 15.0 (Ansys CFX, 2011). It is an implicitly coupled solver that solves the velocity and pressure equations simultaneously. The simulations were run with double precision to minimize the round-off error. To ensure convergence, root mean square (RMS) of residuals and the mass imbalance were set to 1e-5 and 0.001%, respectively. All simulations were performed on high-performance Virgo super cluster available at Indian Institute of Technology Madras. It has a total computing power of 97 TFlops and populated with 2X Intel E5-2670 8C 2.6 GHz processors.

4. Results and discussion

4.1. Grid sensitivity study and numerical validation

The numerical uncertainty caused by the discretization error is evaluated using the grid convergence index (GCI) based on Richardson extrapolation (Roache, 1998). As recommended in the literature, a grid refinement factor (r) of 1.3 was adopted in this study (Celik et al., 2008). Meshes with three different resolution such as fine (6.8 million elements), medium (3.1 million elements) and coarse (1.4 million elements) were generated and the aerodynamic performance parameter (φ), i.e., non-dimensional torque was computed for these grids. The procedure provided by Celik et al. (2008) was followed in this study to estimate the discretization error. The grid refinement was systematically done by varying the global mesh size. The average grid size for a three-dimensional flow domain is expressed as

$$h = \left[\frac{1}{N} \sum_{i=1}^{N} \left(\Delta V_i \right) \right]^{1/3} \tag{5}$$

where ΔV_i is the volume of the ith cell and N is the number of elements in the flow domain. The subscripts 1,2,3 represents fine, medium and coarse meshes, respectively. The apparent order (P) is determined using the equation given below.

$$P = \frac{1}{\ln (r_{21})} \left| \ln \left| \frac{\varepsilon_{32}}{\varepsilon_{21}} \right| + q(P) \right| \tag{6}$$

$$q(P) = \ln \left\{ \frac{r_{21}^p - s}{r_{32}^p - s} \right\}, \text{ where } r_{21} = \frac{h_2}{h_1}, r_{32} = \frac{h_3}{h_2} \tag{7}$$

$$s = 1. \, sign \left\{ \frac{\varepsilon_{32}}{\varepsilon_{21}} \right\}, \text{ where } \varepsilon_{21} = \varphi_2 - \varphi_1, \varepsilon_{32} = \varphi_3 - \varphi_2 \tag{8}$$
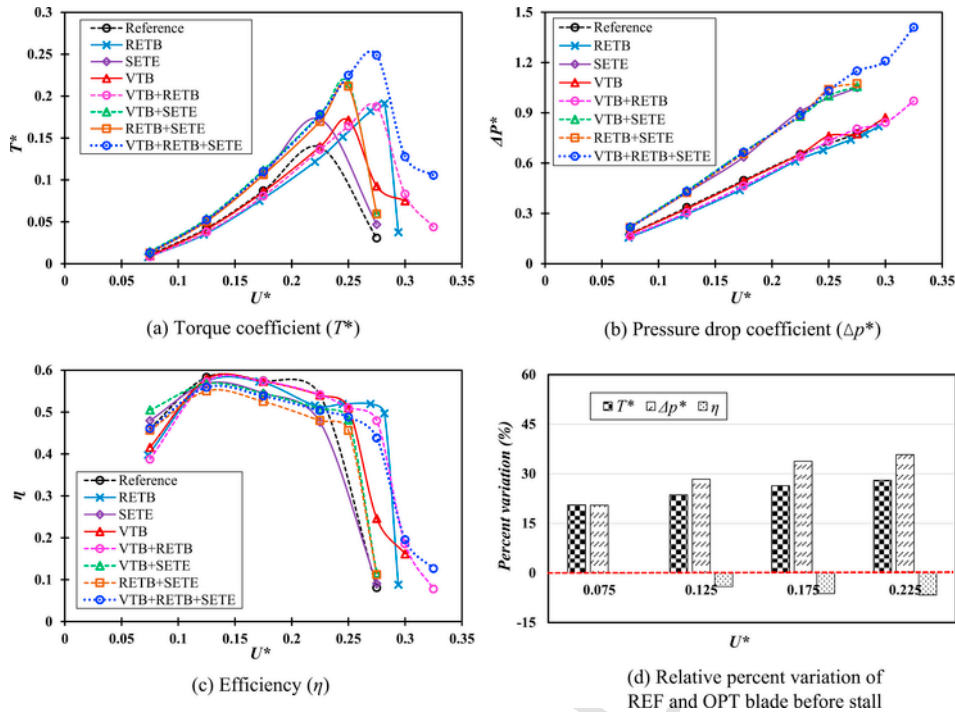
(a) Torque coefficient (*T**)

(b) Pressure drop coefficient (△*p**)

(c) Efficiency (*η*)

(d) Relative percent variation of REF and OPT blade before stall

Fig. 6. Aerodynamic performance comparison of the variants of modified blades with the reference blade.
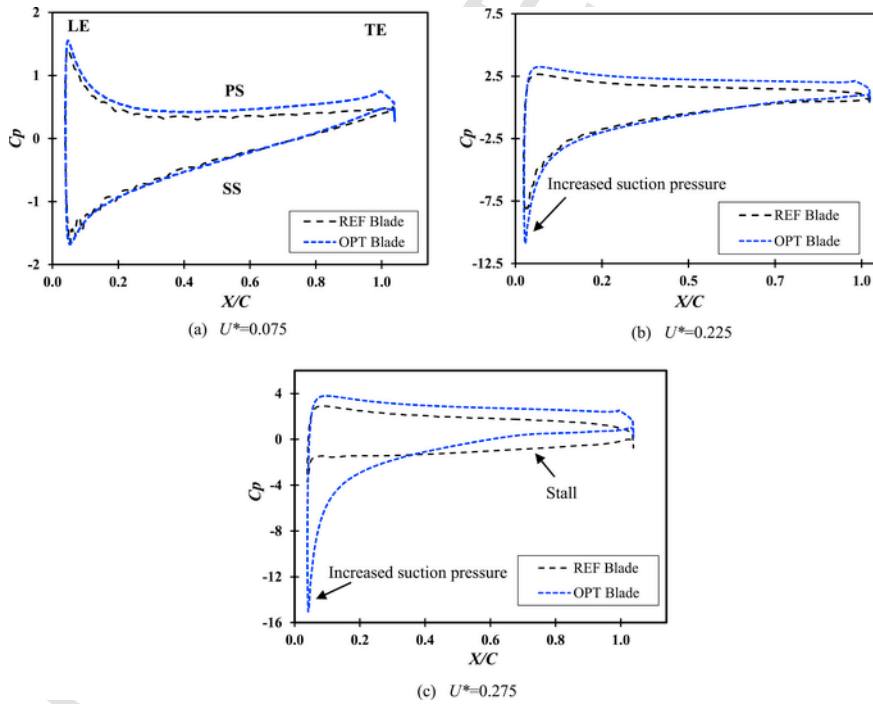

(a) *U**=0.075

(b) *U**=0.225

(c) *U**=0.275

Fig. 7. Comparison of REF and OPT blades for pressure coefficient at blade midspan.

The value of $q(P)$ is 0 in equation (6), since $r_{21} = r_{32} = 1.3$ in this study.

The approximate and extrapolated relative error estimates are computed using equations (9) and (10), respectively.
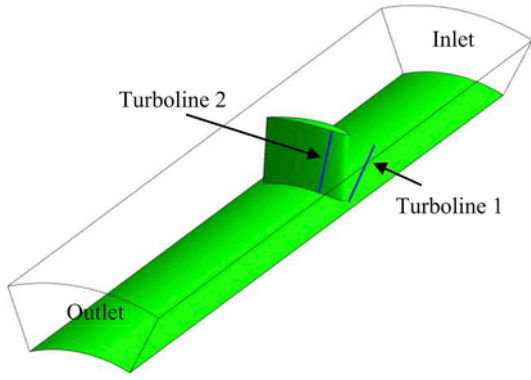
Fig. 8. Location of turbolines.

$$e_a^{21} = \left| \frac{\varphi_1 - \varphi_2}{\varphi_1} \right| \tag{9}$$

$$\varphi_{ext}^{12} = \frac{(r_{21}^p \varphi_1 - \varphi_2)}{(r_{21}^p - 1)} \tag{10}$$

Finally, the GCI is given by

$$GCI_{fine}^{21} = \frac{1.25 * e_a^{21}}{r_{21}^p - 1} \tag{11}$$

Table 4 provides the outcome of GCI analyses. The obtained extrapolated relative errors for the fine and medium grids are 0.35% and 1.52%, respectively. The numerical uncertainty reduces with an increase in grid refinement. The GCI for the medium and fine meshes are 1.92% and 0.43%, respectively. Although the numerical uncertainty in the fine grid is very less, selecting it will increase the computational time considerably. In addition, the GCI between the medium and coarse grid is less than 2%, and it implies that the solution obtained

from the medium grid is not much sensitive to further refinement (Manna et al., 2013). Hence as a trade-off between computational accuracy and time, the medium grid is retained for all computational analyses performed in this study.

To ensure the accuracy of the numerical methodology followed, the present results are compared with experimental results of Curran and Gato (2005) and numerical results of Torresi et al. (2008) and Halder et al. (2015). The nondimensional performance parameters T^*, Δp^*, η are plotted against U^* and the inlet axial velocity (U_A) is varied from 4 to 18 m/s to simulate the entire flow range. Table 5 provides the range of U_A used in the numerical analyses. From Fig. 5, it can be seen that the present numerical results match well with the existing experimental and numerical results. The values $U^* = 0.225$ and $U_A = 14.7312$ m/s correspond to the stall point, after that the torque and efficiency drop rapidly due to flow separation.

4.2. Aerodynamic performance of the modified blades

The aerodynamic performance of the modified blades is shown in Fig. 6. In general, the torque generated by all configurations of modified blades is improved significantly (Fig. 6a). The torque is enhanced for all U^* in SETE combination blades, while it occurred at a relatively higher U^* with delayed stall in RETB combination blades. The reason behind the improved torque of SETE variants can be explained by the increased pressure drop as shown in Fig. 6b. The combined VTB, RETB and SETE blade shows higher torque compared to other variants. Moreover, the efficiency of the modified designs is reduced due to increased pressure drop. Although the efficiency decreases (Fig. 6c), the modified designs show wider operating range excluding the SETE blade, where only the torque is enhanced. As explained earlier, the wider operating range is vital to improve the mean turbine power output. From Fig. 6a, it is evident that the combined VTB, RETB and SETE blade (now onward referred as OPT) is superior to other designs, both in terms of operating range and turbine power output. Fig. 6d shows the relative percent variation of the REF and OPT blade before stall condition. It can be seen that the percent increase in pressure drop is higher than the corresponding torque enhancement. This causes a decrease in the effi-
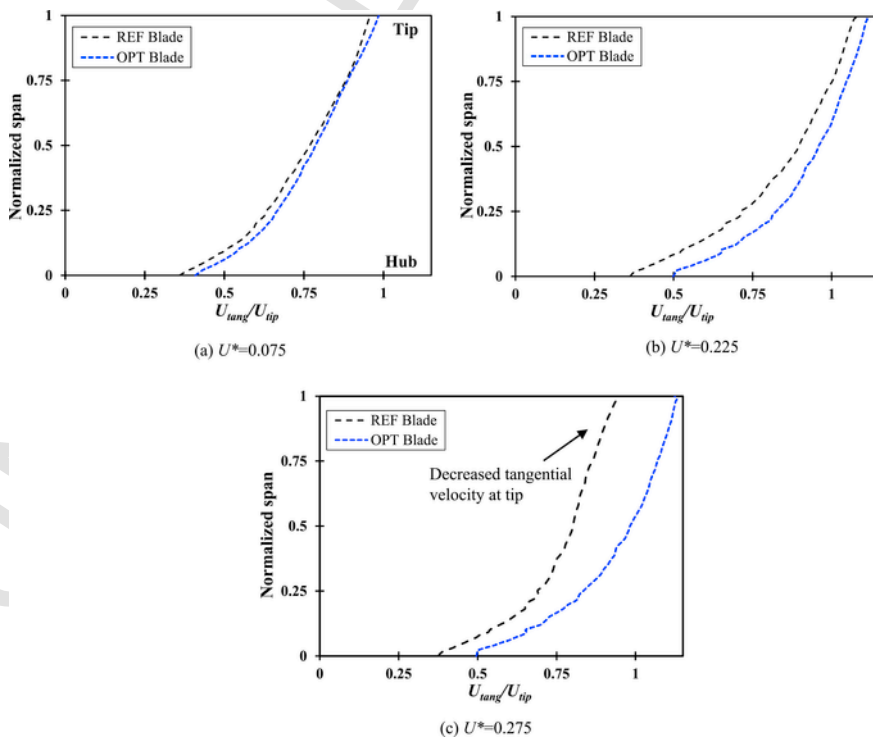

(a) U^*=0.075

(b) U^*=0.225

(c) U^*=0.275

Fig. 9. Spanwise distribution of non-dimensional tangential velocity at turboline 1, for different values of U^*.
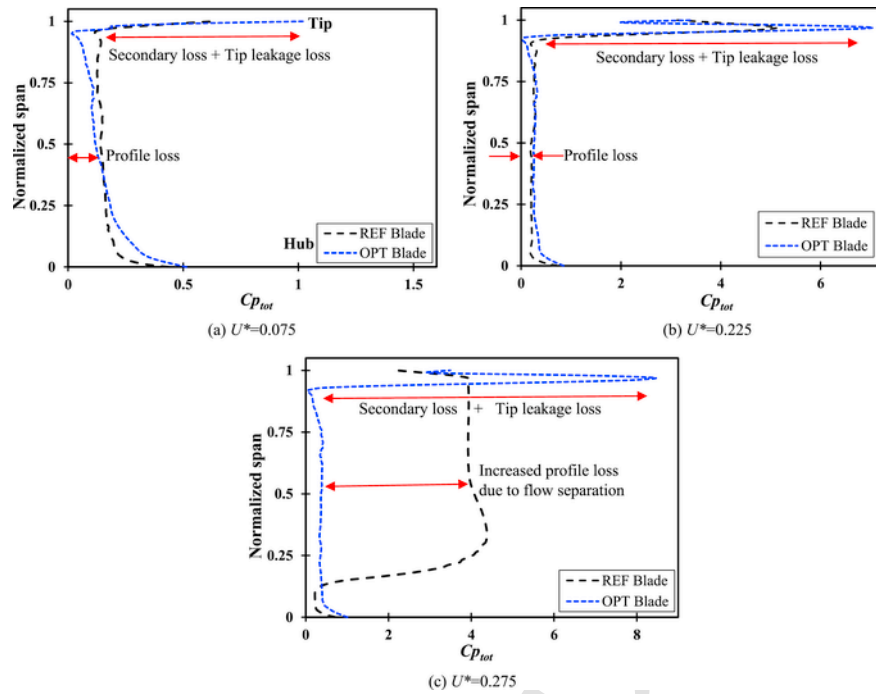
Fig. 10. Total pressure coefficient distribution at turboline 2 on the blade suction side for. REF and OPT blades at different values of U^*.
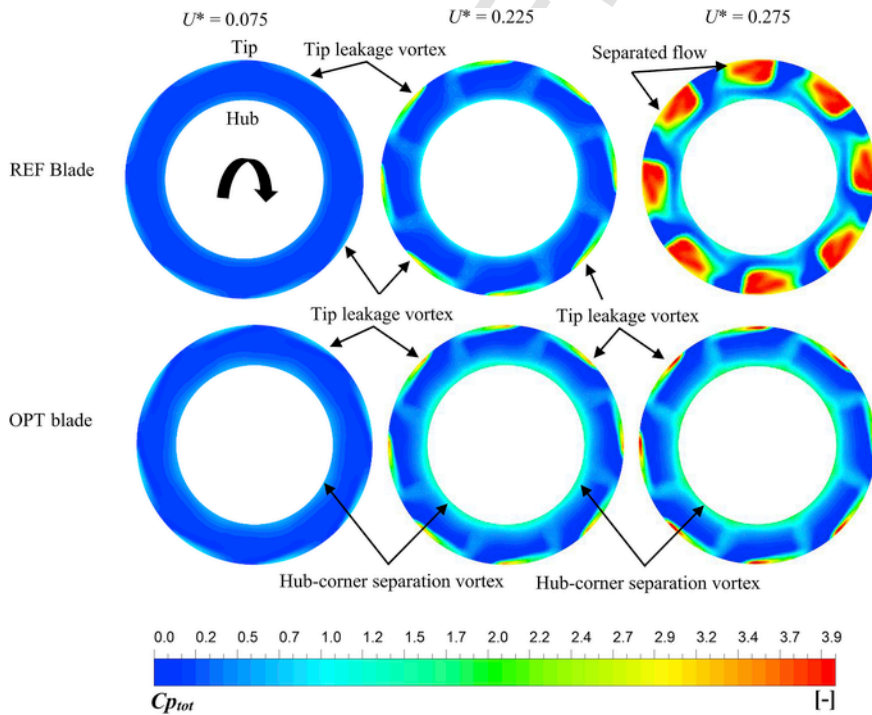

Fig. 11. Full flow domain total pressure coefficient contour at 20%C downstream of blade SS for REF and OPT blades at different values of U^*.

ciency of OPT blade. The decrease in efficiency increases with an increase in U^* as the losses increase significantly with U^*. Further, a detailed flow analysis was carried out to comprehend the fluid flow behavior in the OPT blade.

4.3. Flow analysis

As U^* increases the performance parameter also changes. Therefore, it is required to distinct the effect of performance parameter for REF

and OPT blade. At a higher U^* ($=0.275$) the OPT blade improved the stall limit while the REF blade stalled after U^* ($=0.225$). Furthermore, the performance at low flowrates is also important, hence three different flow coefficients ($U^* = 0.075$, 0.225, and 0.275) were adopted for flowfield comparison of REF and OPT blade. Fig. 7 shows the pressure coefficient (Cp) distribution at blade midspan, and it is expressed by

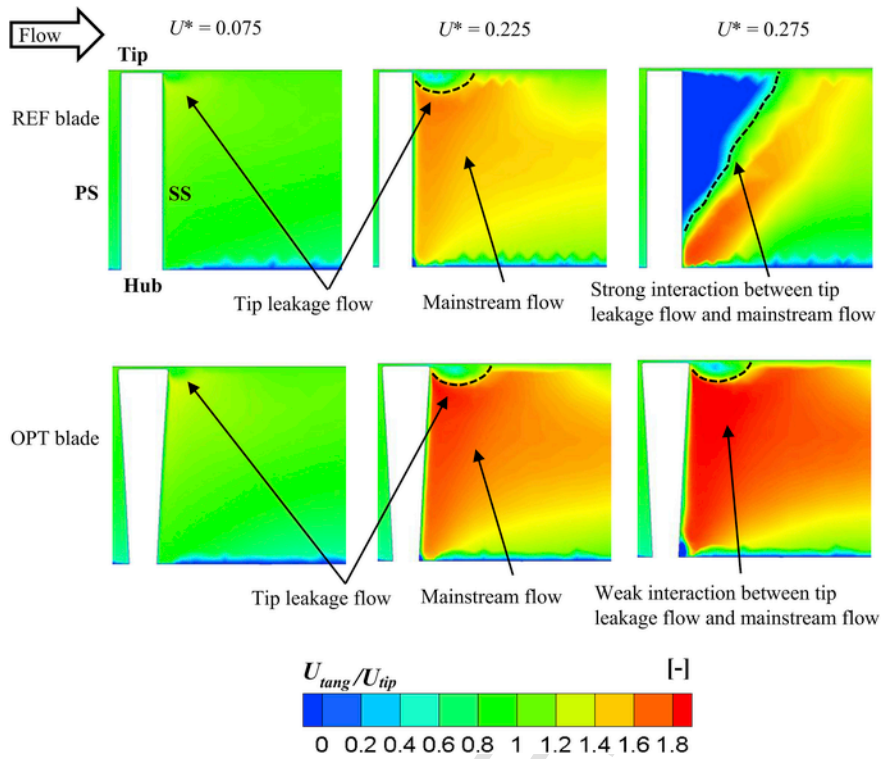$$Cp = \left[\frac{p - p_e}{0.5 \, \rho \, U_A^2} \right] \tag{12}$$

Fig. 12. Non-dimensional tangential velocity contours for REF and OPT blades at the mid chord section at different values of U^*.
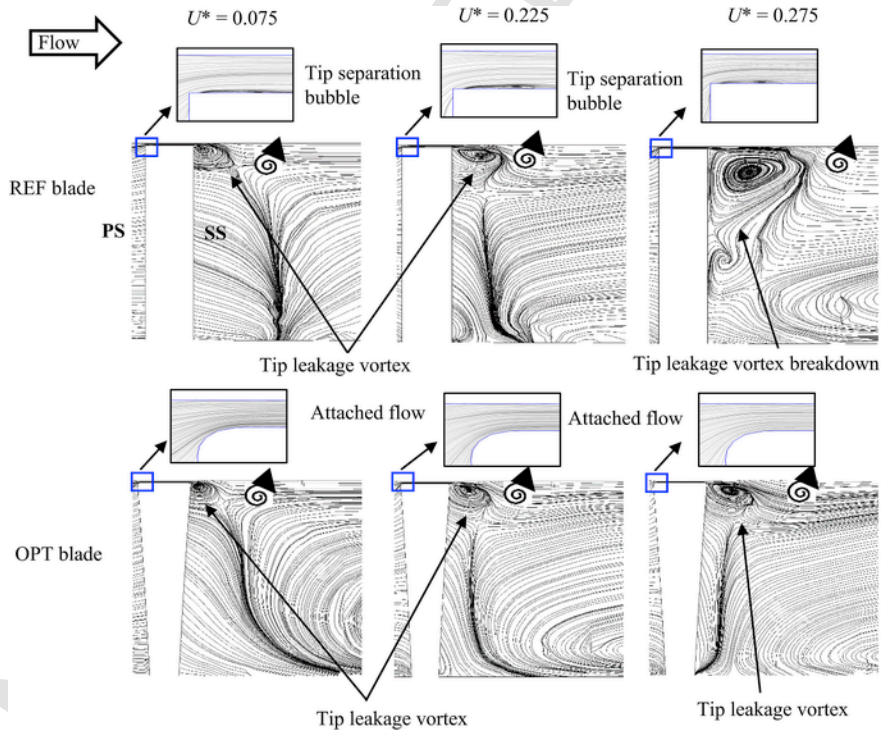

Fig. 13. Streamlines at mid chord section for REF and OPT blades at different values of U^*.

As shown in the figure, the OPT blade shows slightly increased pressure at blade LE and TE for $U^* = 0.075$. The increased blade loading for the OPT blade is significant at $U^* = 0.225$, where a higher suction pressure occurs at LE compared to the reference (REF) blade. The area enclosed by Cp curve represents the blade lift force. Hence, a higher enclosed area signifies increased lift and increased torque in the OPT blade. At higher $U^* (=0.275)$, the suction pressure at LE vanishes in REF blade and it shows constant pressure on the SS which indicates stall. Increased angle of attack (AOA) and the corresponding severe adverse pressure gradient is responsible for stall in REF blade. In contrast, the OPT blade shows increased suction near LE which explains the delayed stall and enhanced torque (Fig. 6a).

Fig. 8 illustrates the location of turbolines along which the tangential velocity and total pressure coefficient distributions are plotted. Fig.
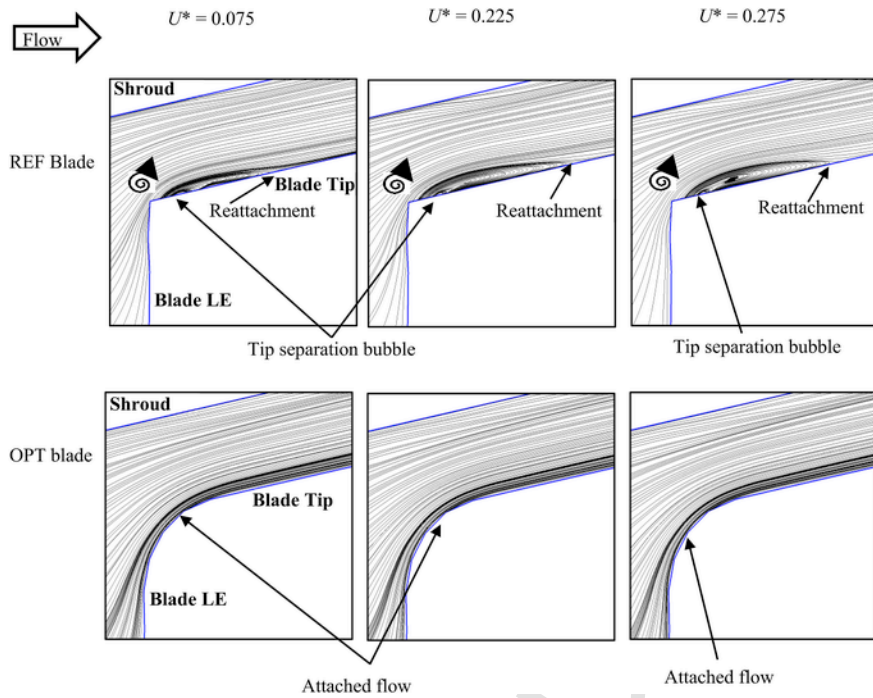
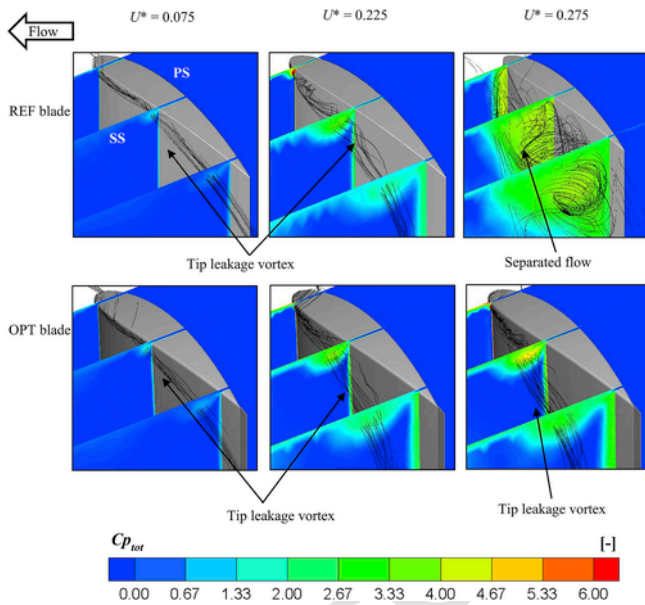**Fig. 14.** Streamlines at blade leading edge for REF and OPT blades at different values of U^*.

Fig. 15. Streamlines at different planes along blade chord for REF and OPT blades at. different values of U^*.

Fig. 16. Tip leakage flow patterns for REF and OPT blades at different values of U^*.

9 represents the spanwise distribution of non-dimensional tangential velocity at turboline 1 (Fig. 8). The tangential velocity is a critical factor that affects the turbine power output as it is evident from the Euler equation ($w_{turbine} = U\left(c_{t1} - c_{t2}\right)$) for turbine. As revealed in the figure, tangential velocity increases from hub to tip for both blades, however the OPT blade shows slight enhancement in tangential velocity at $U^* = 0.075$ as compared to REF blade. The tangential velocity enhancement in OPT blade increases with increase in U^*. The tangential velocity curve steepens, and it is reduced near the tip region for the REF blade due to stall condition at $U^* = 0.275$. In contrast, the OPT blade shows a continuous increase in tangential velocity due to delayed stall (Fig. 6a).
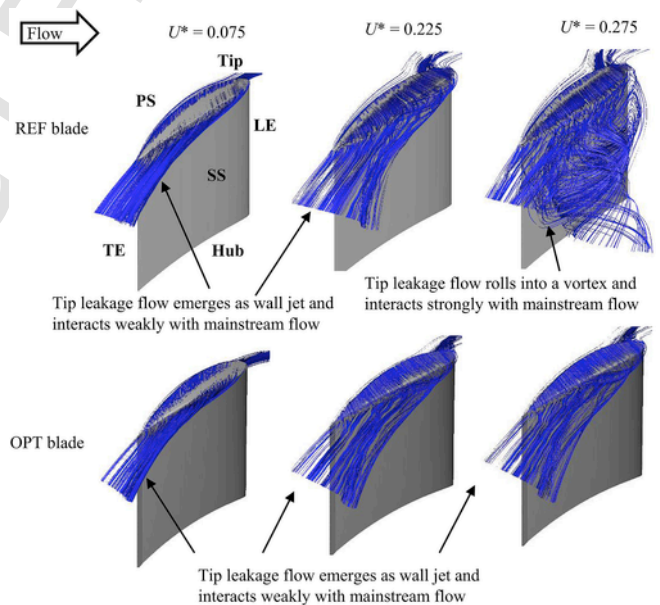
Fig. 10 shows total pressure coefficient distribution at turboline 2 (Fig. 8) located on the blade SS. The total pressure coefficient (Cp_{tot}) can be expressed as

$$Cp_{tot} = \left[\frac{p_{o1} - p_{o2}}{0.5\ \rho\ U_A^2}\right] \tag{13}$$

The losses in turbomachinery can be classified as profile loss, secondary loss and tip leakage loss (Denton, 1993). The profile loss is related to the development of boundary layer, and it increases with flow separation. The secondary loss, also known as end wall loss, arises due to the generation of secondary flows near the endwall. The tip leakage loss occurs due to leakage flow, which arises due to the pressure variation between pressure side (PS) and SS of blade tip. The tip leakage
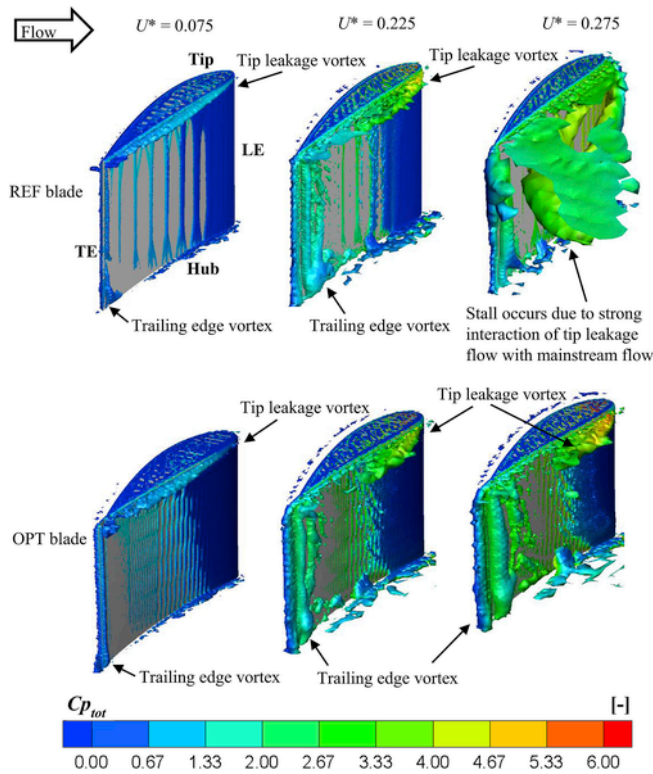
Fig. 17. Isosurface of Q-criterion for a value of 5.5×10^6 s^{-2} with Cp_{tot} distribution for REF and OPT blades at different values of U^*.

loss interacts strongly with secondary loss, and it is difficult to differentiate between them. Hence, they are combined (Niu and Zang, 2011) as shown in Fig. 10. In addition, the Cp_{tot} is higher near the tip region for both the blades and is nearly constant from hub to near-tip region except for the case of blade stall.

At $U^* = 0.075$, the OPT blade shows higher losses near the tip, whereas the profile loss is almost the same for both cases. Due to streamlined entrance, the RET increases TLF and tip leakage loss. This increased tip leakage loss combined with higher pressure drop due to SETE decreases the efficiency of OPT blade (Fig. 6c). The tip leakage loss increases steadily with an increase in U^*. At $U^* = 0.275$, the OPT blade shows an increased loss near the tip region, whereas the REF blade shows an increased loss from about 20% of blade span to tip. The higher profile losses are resulted from flow separation due to adverse pressure gradient, which signifies stall in the REF blade. However, the OPT blade does not show increased profile loss and it implies attached flow.

Fig. 11 shows full flow domain Cp_{tot} contour at 20%C downstream of blade SS. The first impression is a distinctly high Cp_{tot} that is observed near the tip and the hub region. The high Cp_{tot} in the tip and hub region corresponds to the tip leakage vortex (TLV) and the hub-corner separation vortex, respectively. The increase in Cp_{tot} with U^* indicates an increase in tip leakage loss due to increased TLF. The tip leakage loss is higher in the OPT blade compared to the REF blade, due to increased blade loading. At $U^* = 0.275$, a significantly high Cp_{tot} region along the blade span implies stall in REF blade, whereas it is confined near the tip of the OPT blade and indicates delayed stall.

Fig. 12 illustrates non-dimensional tangential velocity contours at the mid-chord section. The low tangential velocity region visible on the SS of blade tip signifies TLF and it increases with an increase in U^* for both blades. In addition, the high-velocity region on the blade SS implies the mainstream flow. The TLF offers blockage to the mainstream

flow and it intensifies with the increase in U^*. The OPT blade shows a higher tangential velocity along the blade span throughout the flow range and it corroborates with the results shown in (Fig. 9). At $U^* = 0.275$ for the REF blade, a low-velocity region is visible on blade SS and it extends from 20% of blade span to tip. It indicates a stall due to the strong interaction between TLF and mainstream flow thereby increased blockage. On the contrary, for OPT blade, the above-mentioned interactions are weak, and confined to a smaller region, thereby reducing blockage and improved the performance.

The flow structures and streamlines at the blade mid-chord section are visualized to comprehend the flow dynamics in the REF and the OPT blade (Fig. 13). The leakage flow ejects from the blade tip PS to SS as a result of pressure difference and rolls down into a clockwise TLV. At a lower $U^* = 0.075$, the TLV is confined near the blade tip SS for both blades. The size of the TLV increases with increase in U^*, because of increased axial velocity and AOA. For both blades, the TLV is confined near the tip region and the mainstream flow is not affected significantly for $U^* \leq 0.225$. With further increase in U^*, the TLV breaks down because of severe adverse pressure gradient in the REF blade and interacts strongly with mainstream flow inducing a stall phenomenon. In contrary, the OPT blade shows a stable TLV and weak mixing with the mainstream flow, which is consistent with the results shown in Fig. 12. The increased TLF due to RET decreases the effective AOA and reduces the adverse pressure gradient, thereby delays the stall.

Further, the tip separation bubble vanishes in OPT blade due to radiused edge in contrast to the REF blade which shows separation bubble near the LE sharp corner (Figs. 13 and 14). In OPT blade, the absence of the separation bubble eliminates blockage to the clearance flow and the leakage loss is increased. The leakage loss is reduced in REF blade due to blockage by separation bubble. These results are consistent with the increased tip leakage loss as shown in Fig. 10. Moreover, the radiused edge in OPT blade prevents tip separation and reduces the intensity of leakage flow interaction with the mainstream flow because of the streamlined edges compared to the sharp edges in the REF blade (Ameri and Bunker, 1999).

Fig. 15 shows the TLV and Cp_{tot} contours at 20%, 50% and 80% planes along the blade chord. It can be observed that the TLV emanates from the LE on the blade SS and diffuses as it moves downstream. A high Cp_{tot} region visible on the SS of chordwise planes indicates TLV. The strength of TLV increases with increase of U^* up to 0.225 and increased Cp_{tot} appears near the SS of blade tip for both blades. For the REF blade, at $U^* = 0.275$ the TLV breaks down and interacts strongly with mainstream flow thereby increasing blockage and causing stall. Severe adverse pressure gradient stems from increased U^* is responsible for the TLV breakdown. In contrast, the TLV is stable in the OPT blade and it interacts weakly with mainstream flow. This explains the delayed stall phenomenon and increased operating range for the OPT blade. Additionally, volumetric streamlines around the blade tip are presented in Fig. 16 to understand the TLF pattern. The TLF emerges as a flat wall jet and interacts weakly with mainstream flow up to $U^* \leq 0.225$ for both blades. However, at $U^* = 0.275$, the REF blade shows strong interaction between the TLF and mainstream flow in contrast to the OPT blade. This corroborates the results shown in Figs. 12 and 15.

Fig. 17 shows the isosurface of Q-criterion ($Q = 5.5 \times 10^6$ s^{-2}) coloured with Cp_{tot}. As explained earlier, the TLV is visible on the blade SS, and the TE vortex originates from the blade TE. The increased Cp_{tot} along the blade SS and TE also indicates the aforementioned vortices. Both the TLV and TE vortex increase in size with U^*. The TLV is confined near the tip region and there is no significant interaction with the mainstream flow for both blades up to $U^* = 0.225$. At $U^* = 0.275$, the TLV breaks down in REF blade and interacts strongly with mainstream flow. It increases blockage and stall occurs. However, in the OPT blade, TLV is stable and interacts weakly with mainstream flow thereby delaying stall.

5. Conclusion

The aerodynamic performance of Wells turbine using various combination of design modifications was computed numerically. The design modifications implemented in this study were radiused edge tip, static extended trailing edge and variable thickness along the blade span. The optimum design was selected based on the wider operating range and maximum power output. Moreover, a detailed flow field analysis of the optimum design was presented using the pressure coefficient, total pressure coefficient, tangential velocity, and tip leakage flow. The main conclusions are:

- The combined radiused edge tip, static extended trailing edge, and variable blade thickness provided wider operating range and enhanced power output.
- The combined design improved the relative stall margin and turbine power by 22% and 97%, respectively and decreased relative efficiency by 7.7%.
- The increased suction pressure in the combined design is responsible for the enhanced power output.
- The nature of the interaction between TLF and mainstream flow dictates the Wells turbine performance. The above-said interactions are weak in the combined design and are responsible for the delayed stall.
- Moreover, further investigations should be carried out to comprehend the effects of design parameters on the performance with a multi-objective optimization approach.

Uncited References

CFXANSYS, 2011.

References

Ameri, A.A., Bunker, R.S., 1999. Heat transfer and flow on the first-stage blade tip of a power generation gas turbine: Part 2 — simulation results. ASME 1999 Int. Gas Turbine Aeroengine Congr. Exhib. 122, 272–277. https://doi.org/10.1115/99-GT-283.

Ansys 2012. ICEM CFD. "15.0. Ansys." Inc. Southpointe.

Astariz, S., Iglesias, G., 2015. The economics of wave energy: a review. Renew. Sustain. Energy Rev. 45, 397–408. https://doi.org/10.1016/j.rser.2015.01.061.

Celik, I.B., Ghia, U., Roache, P.J., Freitas, C.J., Coleman, H., Raad, P.E., 2008. Procedure for estimation and reporting of uncertainty due to discretization in CFD applications. J. Fluids Eng. 130, https://doi.org/10.1115/1.2960953.

Ansys CFX, 2011. Solver Theory Guide. Ansys." Inc., Canonsburg, PA.

Cui, Y., Hyun, B.-S., 2016. Numerical study on Wells turbine with penetrating blade tip treatments for wave energy conversion. Int. J. Nav. Archit. Ocean Eng. https://doi.org/10.1016/j.ijnaoe.2016.05.009.

Curran, R., Gato, L.M.C., 2005. The energy conversion performance of several types of Wells turbine designs. Proc. Inst. Mech. Eng. Part A J Power Energy 211, 133–145. https://doi.org/10.1243/0957650971537051.

Denton, J.D., 1993. Loss mechanisms in turbomachines. In: ASME 1993 Int Gas Turbine Aeroengine Congr Expo. https://doi.org/10.1115/93-GT-435.

Falcão, AF. d. O., 2010. Wave energy utilization: a review of the technologies. Renew. Sustain. Energy Rev. 14, 899–918. https://doi.org/10.1016/j.rser.2009.11.003.

Gato, L.M.C., 1990. Performance of the Wells turbine with a double row of guide vanes. JSME Int. J. Ser. 2 Fluids Eng. Heat Transf. Power Combust. Thermophys. Prop. 33 (2), 265–271. https://doi.org/10.1299/jsmeb1988.33.2_265.

Gato, L.M.C., Webster, M., 2001. An experimental investigation into the effect of rotor blade sweep on the performance of the variable-pitch Wells turbine. Proc. Inst. Mech. Eng. Part A J Power Energy 215, 611–622. https://doi.org/10.1243/0957650011538848.

Govardhan, M., Dhanasekaran, T.S., 2002. Effect of guide vanes on the performance of a self-rectifying air turbine with constant and variable chord rotors. Renew. Energy 26 (2), 201–219. https://doi.org/10.1016/S0960-1481(01)00124-0.

Halder, P., Samad, A., Kim, J.H., Choi, Y.S., 2015. High performance ocean energy harvesting turbine design-A new casing treatment scheme. Energy 86, 219–231. https://doi.org/10.1016/j.energy.2015.03.131.

Halder, P., Samad, A., Thevenin, D., 2017. Improved design of a Wells turbine for higher operating range. Renew. Energy 106, 122–134. https://doi.org/10.1016/j.renene.2017.01.012.

Halder, P., Mohamed, M.H., Samad, A., 2018. Wave energy conversion: design and shape optimization. Ocean Eng. 150, 337–351. https://doi.org/10.1016/j.oceaneng.2017.12.072.

Hu, Q., Li, Y., 2018. Unsteady RANS simulations of Wells turbine under transient flow conditions. J. Offshore Mech. Arct. Eng. 140, https://doi.org/10.1115/1.4037696.

Kumar, P.M., Halder, P., Samad, A., 2018 Jun 17. Performance analysis of Wells turbine with radiused blade tip. In: ASME 2018 37th International Conference on Ocean, Offshore and Arctic Engineering. American Society of Mechanical Engineershttps://doi.org/10.1115/OMAE2018-78668, V010T09A049-V010T09A049.

Liu, T., Kuykendoll, K., Rhew, R., Jones, S., 2006. Avian wing geometry and kinematics. AIAA J. 44, 954–963. https://doi.org/10.2514/1.16224.

Liu, T.S., Montefort, J., Liou, W., Pantula, S.R., Shams, Q.A., 2007. Lift enhancement by static extended trailing edge. J. Aircr. 44, 1939–1947. https://doi.org/10.2514/1.31995.

Manna, P., Dharavath, M., Sinha, P.K., Chakraborty, D., 2013. Optimization of a flight-worthy scramjet combustor through CFD. Aero. Sci. Technol. 27, 138–146. https://doi.org/10.1016/j.ast.2012.07.005.

Menter, F.R., 1994. Two-equation eddy-viscosity turbulence models for engineering applications. AIAA J. 32, 1598–1605. https://doi.org/10.2514/3.12149.

Mohamed, M.H., Janiga, G., Pap, E., Thévenin, D., 2011. Multi-objective optimization of the airfoil shape of Wells turbine used for wave energy conversion. Energy 36, 438–446. https://doi.org/10.1016/j.energy.2010.10.021.

Mustapa, M.A., Yaakob, O.B., Ahmed, Y.M., Rheem, C.K., Koh, K.K., Adnan, F.A., 2017. Wave energy device and breakwater integration: a review. Renew. Sustain. Energy Rev. 77, 43–58. https://doi.org/10.1016/j.rser.2017.03.110.

Nazeryan, M., Lakzian, E., 2018. Detailed entropy generation analysis of a Wells turbine using the variation of the blade thickness. Energy 143, 385–405. https://doi.org/10.1016/j.energy.2017.11.006.

Niu, M., Zang, S., 2011. Experimental and numerical investigations of tip injection on tip clearance flow in an axial turbine cascade. Exp. Therm. Fluid Sci. 35, 1214–1222. https://doi.org/10.1016/j.expthermflusci.2011.04.009.

Raghunathan, S., 1995. The Wells air turbine for wave energy conversion. Prog. Aero. Sci. 31 (4), 335–386. https://doi.org/10.1016/0376-0421(95)00001-F.

Raghunathan, S., Beattie, W.C., 1996 Dec. Aerodynamic performance of contra-rotating Wells turbine for wave energy conversion. Proc. IME J. Power Energy 210 (6), 431–447. https://doi.org/10.1243/PIME_PROC_1996_210_071_02.

Raghunathan, S., Tan, C.P., 1983 Nov. Performance of biplane Wells turbine. J. Energy 7 (6), 741–742. https://doi.org/10.2514/3.62727.

Roache, P.J., 1998 May. Verification of codes and calculations. AIAA J. 36 (5), 696–702 https://doi.org/10.2514/2.457.

Shaaban, S., 2017 Oct 10. Wells turbine blade profile optimization for better wave energy capture. Int. J. Energy Res. 41 (12), 1767–1780. https://doi.org/10.1002/er.3745.

Shaaban, S., Hafiz, A.A., 2012. Effect of duct geometry on Wells turbine performance. Energy Convers. Manag. 61, 51–58. https://doi.org/10.1016/j.enconman.2012.03.023.

Shehata, A.S., Xiao, Q., Saqr, K.M., Alexander, D., 2017. Wells turbine for wave energy conversion: a review. Int. J. Energy Res. 41, 6–38. https://doi.org/10.1002/er.3583.

Taha, Z., Sugiyono, Tuan Ya TMYS., Sawada, T., 2011. Numerical investigation on the performance of Wells turbine with non-uniform tip clearance for wave energy conversion. Appl. Ocean Res. 33, 321–331. https://doi.org/10.1016/j.apor.2011.07.002.

Takao, M., Setoguchi, T., Kinoue, Y., Kaneko, K., 2007. Wells turbine with end plates for wave energy conversion. Ocean Eng. 34, 1790–1795. https://doi.org/10.1016/j.oceaneng.2006.10.009.

Torresi, M., Camporeale, S.M., Strippoli, P.D., Pascazio, G., 2008. Accurate numerical simulation of a high solidity Wells turbine. Renew. Energy 33, 735–747. https://doi.org/10.1016/j.renene.2007.04.006.

Torresi, M., Camporeale, S.M., Pascazio, G., 2009. Detailed CFD analysis of the steady flow in a Wells turbine under incipient and deep stall conditions. J. Fluids Eng. 131, https://doi.org/10.1115/1.3155921.